1 **Localising individual atoms of tryptophan side chains in the metallo-β-lactamase IMP-1**

2 **by pseudocontact shifts from paramagnetic lanthanoid tags at multiple sites**

3 Henry W. Orton,[a,*] Iresha D. Herath,[b,*] Ansis Maleckis,[c] Shereen Jabar,[b] Monika Szabo,[d] Bim

4 Graham,[d] Colum Breen,[e] Lydia Topping,[e] Stephen J. Butler,[e] Gottfried Otting[a]

6 [a] ARC Centre of Excellence for Innovations in Peptide & Protein Science, Research School of

7 Chemistry, Australian National University, Canberra, ACT 2601, Australia

8 [b] Research School of Chemistry, The Australian National University, Sullivans Creek Road,

9 Canberra ACT 2601, Australia

10 [c] Latvian Institute of Organic Synthesis, Aizkraukles 21, LV-1006 Riga, Latvia

11 [d] Monash Institute of Pharmaceutical Sciences, Monash University, Parkville, VIC 3052,

12 Australia

13 [e] Department of Chemistry, Loughborough University, Epinal Way, Loughborough, LE11

14 3TU, United Kingdom

19 Correspondence: Gottfried Otting (gottfried.otting@anu.edu.au)

20 [*] These authors contributed equally to this work.

22 **Abstract**

23 The metallo-β-lactamase IMP-1 features a flexible loop near the active site that assumes

24 different conformations in single crystal structures, which may assist in substrate binding and

25 enzymatic activity. To probe the position of this loop, we labelled the tryptophan residues of

26 IMP-1 with 7-^{13}C-indole and the protein with lanthanoid tags at three different sites. The

27 magnetic susceptibility anisotropy ($\Delta\chi$) tensors were determined by measuring pseudocontact

28 shifts (PCS) of backbone amide protons. The $\Delta\chi$ tensors were subsequently used to identify

29 the atomic coordinates of the tryptophan side chains in the protein. The PCSs were sufficient

30 to determine the location of Trp28, which is located in the active site loop targeted by our

31 experiments, with high accuracy. Its average atomic coordinates showed barely significant

32 changes in response to the inhibitor captopril. It was found that localisation spaces could be

33 defined with better accuracy by including only the PCSs of a single paramagnetic lanthanoid

34 ion for each tag and tagging site. The effect was attributed to the shallow angle with which

35 PCS isosurfaces tend to intersect if generated by tags and tagging sites that are identical except
36 for the paramagnetic lanthanoid ion.
37
1 Introduction

39 The metallo-β-lactamase IMP-1 is an enzyme that hydrolyses β-lactams, thus conferring
40 penicillin resistance to bacteria. First identified 30 years ago in the Gram-negative bacteria in
41 early 1990s from *Pseudomonas aeruginosa* and *Serratia marcescens* (Bush 2013), IMP-1 has
42 become a serious clinical problem due to horizontal gene transfer by a highly mobile gene
43 (*bla*$_{IMP-1}$) located on an integron (Arakawa et al., 1995), as the *bla*$_{IMP-1}$ gene has been detected
44 in isolates of *Klebsiella pneumoniae*, *Pseudomonas putida*, *Alcaligenes xylosoxidans*,
45 *Acinetobacter junii*, *Providencia rettgeri*, *Acinetobacter baumannii* and *Enterobacter*
46 *aerogenes* (Ito et al., 1995; Laraki et al., 1999a; Watanabe et al., 1991). Critically, IMP-1
47 confers resistance also to recent generations of carbapenems and extended-spectrum
48 cephalosporins (Laraki et al., 199b; Bush et al., 2010; van Duin et al., 2013).
49 Multiple crystal structures have been solved of IMP-1, free and in complex with various
50 inhibitors (Concha et al., 2000; Toney et al., 2001; Moali et al., 2003; Hiraiwa et al., 2014;
51 Brem et al., 2016; Hinchliffe et al., 2016; 2018; Wachino et al., 2019; Rossi et al., 2021). IMP-
52 1 belongs to the subclass B1 of metallo-β-lactamases, which contain two zinc ions bridged by
53 the sulfur atom of a cysteine residue in the active site (Concha, 2000). One of Zn^{2+} ions can
54 readily be replaced by a Fe^{3+} ion (Carruthers et al., 2014). The active site is flanked by a loop
55 (referred to as L3 loop) that contains a highly solvent-exposed tryptophan residue surrounded
56 by glycine residues on either side. Both the loop and the tryptophan residue (Trp28 in the IMP-
57 1-specific numbering used by Concha et al. (2000) and Trp64 in the universal numbering
58 scheme by Galleni et al. (2001)) assume different conformations in different crystal structures,
59 suggesting that the loop acts as a mobile flap to cover bound substrate (Fig. 1). The L3 loop
60 and the functional implication of its flexibility has been studied extensively for different
61 metallo-β-lactamases containing the Gly-Trp-Gly motif in the loop (Huntley et al., 2000; 2003;
62 Moali et al., 2003; Yamaguchi et al., 2015; Palacios et al., 2019; Gianquinto et al., 2020; Softley
63 et al., 2020). Flexibility of the L3 loop is a general feature also of many metallo-β-lactamases
64 without the Gly-Trp-Gly motif and is thought to contribute to the wide range of β-lactam
65 substrates that can be hydrolyzed by the enzymes (González et al., 2016; Linciano et al., 2019;
66 Salimraj et al., 2018). In the case of the metallo-β-lactamase from *B. fragilis*, which is closely
67 related to IMP-1, electron density could be detected for the Gly-Trp-Gly motif in the crystal

68   structure of the protein in the presence (Payne et al., 2003) but not absence of an inhibitor

69   (Concha et al., 1996), and an NMR relaxation study in solution confirmed the increased

70   flexibility of both the L3 loop and, in particular, the sidechain of the tryptophan residue

71   (Huntley et al., 2000). A similar situation prevails in the case of the IMP-1 variant IMP-13,

72   where different crystal structures of the ligand-free protein show the L3 loop in very different

73   conformations, sometimes lacking electron density, while NMR relaxation measurements

74   confirmed the increased flexibility of the loop (Softley et al., 2020).

75   Due to the rigidity of their sidechains, tryptophan residues frequently contribute to the

76   structural stability of three-dimensional protein folds and it is unusual to observe tryptophan

77   sidechains fully solvent-exposed as in the Gly-Trp-Gly motif of substrate-free IMP-1. The

78   functional role of Trp28 in IMP-1 was assessed in an early mutation study by mutating Trp28

79   to alanine and, in a different experiment, eliminating the L3 loop altogether. Enzymatic activity

80   measurements revealed an increase in the Michaelis constant K_m and a decrease in k_{cat}/K_m ratios

81   for all β-lactams tested, illustrating the importance of the Trp28 sidechain for catalytic activity.

82   Complete removal of the L3 loop reduced the k_{cat}/K_m ratios even further, but without

83   completely abolishing the enzymatic activity (Moali et al., 2003).

84

85
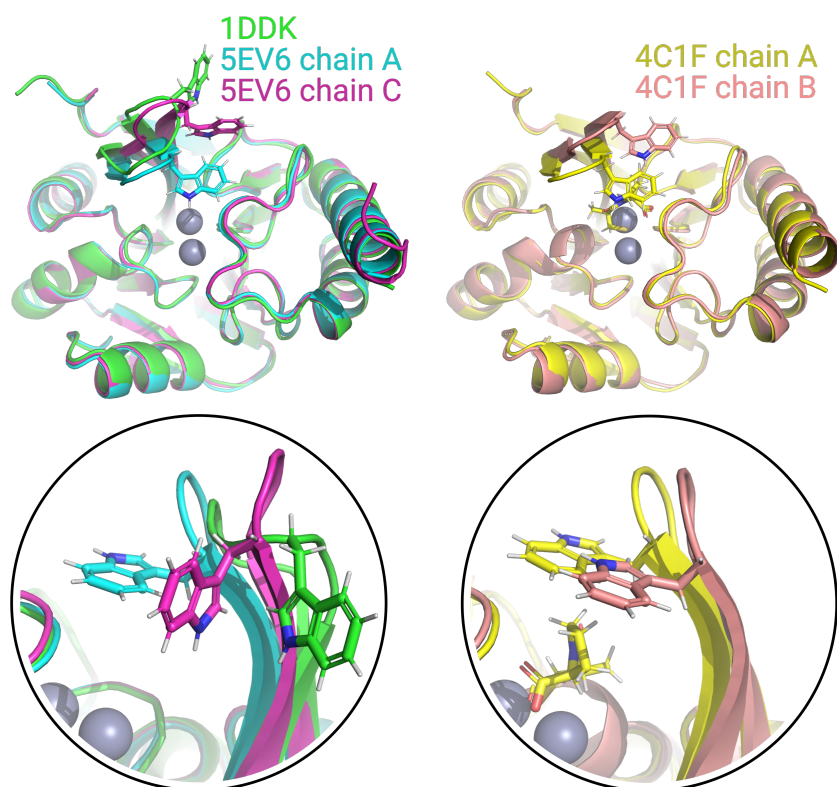
Figure 1. Superimposition of crystal structures of IMP-1 showing structural variation of Trp28 and the associated loop L3. The structures shown are of the Zn^{2+}/Zn^{2+} complex without inhibitor (green, PDB ID 1DDK, Concha et al., 2000; cyan for chain A and magenta for chain C, PDB ID 5EV6, Hinchliffe et al., 2016), with bound L-captopril (yellow for chain A and salmon for chain B, PDB ID 4CIF, Brem et al., 2016). Zn^{2+} ions are represented by grey spheres and bound captopril is shown in the structure 4C1F chain A.

In the crystalline state, the conformation of a solvent-exposed loop is easily impacted by crystal packing forces. Therefore, it is unclear what the actual conformation of the L3 loop is in solution. To address this question, we used solution NMR spectroscopy to assess the location of Trp28 in IMP-1 both in the absence and presence of the inhibitor L-captopril, which inhibits metallo-β-lactamases by binding to the active-site zinc ions (Brem et al., 2016). The analysis was hindered by incomplete backbone resonance assignments of IMP-1 attributed to

100 conformational exchange processes in parts of the protein (Carruthers et al., 2014). As it is
101 difficult to accurately position the atoms of a solvent-exposed polypeptide loop in solution by
102 nuclear Overhauser effects (NOE), we used pseudocontact shifts (PCS) generated by
103 lanthanoid ions attached at different sites of IMP-1 to determine the location of Trp28 relative
104 to the core of the protein. PCSs generated by multiple different paramagnetic metal ions or the
105 same metal ion attached at different sites of a protein have previously been shown to allow
106 localizing atoms at remote sites of interest, such as in specific amino acid side chains (Pearce
107 et al., 2017; Lescanne et al., 2018), bound ligand molecules (Guan et al., 2013; Chen et al.,
108 2016) or proteins (Pintacuda et al., 2006; Keizers et al., 2010; de la Cruz et al., 2011;
109 Kobashigawa et al., 2012; Brewer et al., 2015) or for 3D structure determinations of proteins
110 (Yagi et al., 2013; Crick et al., 2015; Pilla et al., 2017).

111   IMP-1 contains six tryptophan residues, each containing several aromatic hydrogens
112 with similar chemical shifts. To increase the spectral resolution in the 2D NMR spectra
113 recorded for PCS measurements, we labelled each tryptophan sidechain with a single ^{13}C atom
114 by expressing the protein in the presence of 7-^{13}C-indole (Maleckis et al., 2021). The results
115 show that the localization spaces defined by the tryptophan PCSs fully agree with previously
116 determined crystal structures of IMP-1 for all tryptophan residues. They suggest little change
117 in the average conformation of the L3 loop upon binding of captopril. The results illustrate the
118 accuracy with which the positions of individual atoms can be determined by PCSs from
119 lanthanoid tags even in proteins of limited stability.

120

121 **2 Experimental procedures**
122 **2.1 Production, purification and tagging of proteins**
123 **2.1.1 Plasmid constructs and ^{13}C-labelled indole**
124 Three different cysteine mutations (A53C, N172C and S204C) were introduced into the bla_{IMP1}
125 gene in the pET-47b(+) plasmid using a modified QuikChange protocol (Qi and Otting, 2019).
126 Deuterated 7-^{13}C-indole was synthesized as described with deuteration in all positions other
127 than position 7 (Maleckis et al., 2021). The amino acid sequence of the protein was that
128 reported in the crystal structure 4UAM (Carruthers et al., 2014), except that the N-terminal
129 alanine residue was substituted by a methionine to avoid heterogeneity by incomplete
130 processing by amino peptidase.

131

132 **2.1.2 Protein production**

133   Uniformly ^{15}N-labelled samples of the cysteine mutants of IMP-1 were expressed in *E. coli*
134   BL21(DE3) cells. The cells were grown at 37 °C in Luria–Bertani (LB) medium containing 50
135   mgL^{-1} kanamycin until the OD$_{600}$ reached 0.6–0.8 and were then transferred to 300 mL of M9
136   medium (6 gL^{-1} Na$_2$HPO$_4$, 3 gL^{-1} KH$_2$PO$_4$, 0.5 gL^{-1} NaCl, pH 7.2) supplemented with 1 gL^{-1}
137   of ^{15}NH$_4$Cl. After induction with isopropyl-β-D-thiogalactopyranoside (IPTG, final
138   concentration 1 mM), the cells were incubated at room temperature for 16 hours. Following
139   centrifugation, the cells were resuspended in buffer A (50 mM HEPES, pH 7.5, 100 μM ZnSO$_4$)
140   for lysis by a homogeniser (Avestin Emulsiflex C5). The supernatant of the centrifuged cell
141   lysate was loaded onto a 5 mL SP column, the column was washed with 20 column volumes
142   buffer B (same as buffer A but with 50 mM NaCl) and the protein was eluted with a gradient
143   of buffer C (same as buffer A but with 1 M NaCl).

144   IMP-1 samples containing 7-^{13}C-tryptophan were produced by continuous exchange
145   cell-free protein synthesis (CFPS) from PCR-amplified DNA with eight-nucleotide single-
146   stranded overhangs as described (Wu et al., 2007), using 7-^{13}C-indole as a precursor for the *in*
147   *vitro* production of tryptophan (Maleckis2021). The CFPS reactions were conducted at 30 ºC
148   for 16 h using 1 mL inner reaction mixture and 10 mL outer buffer. Tryptophan was omitted
149   from the mixture of amino acids provided and deuterated 7-^{13}C-indole was added from a stock
150   solution in 50 % DMSO/50 % H$_2$O to the inner and outer buffers at a final concentration of
151   0.75 mM. The protein samples were purified as described above. ~5 mg of the indole was
152   required for preparing each NMR sample.
153

154   **2.1.3 Ligation with C2-Ln^{3+} tag**
155   To ensure the reduced state of cysteine thiol groups, the protein samples were treated with 2
156   mM dithiothreitol (DTT) for 1 hour. Subsequently, the DTT was removed using an Amicon
157   ultrafiltration centrifugal tube with a molecular weight cut-off of 10 kDa, concentrating the
158   protein samples to 50 μM in buffer A. The samples were incubated overnight at room
159   temperature with shaking in the presence of five-fold molar excess of C2 tag (Graham et al.,
160   2011; de la Cruz et al., 2011) loaded with either Y^{3+}, Tb^{3+} or Tm^{3+}. Following the tagging
161   reaction, the samples were washed using an Amicon centrifugal filter unit to remove unbound
162   tag and the buffer was exchanged to NMR buffer (20 mM MES, pH 6.5, 100 mM NaCl).
163

164   **2.1.4 Ligation with C12-Ln^{3+} tag**

165 The ligation reaction of IMP-1 N172C with the C12-Ln^{3+} tag loaded with either Y^{3+}, Tb^{3+} or
166 Tm^{3+} (Herath et al., 2021) was conducted in the same way as with the C2-Ln^{3+} tags, except that
167 the reactions were carried out in buffer A with the pH adjusted to 7.0.
168
169 **2.2 NMR spectroscopy**
170 All NMR data were acquired at 37 °C on Bruker 600 and 800 MHz NMR spectrometers
171 equipped with TCI cryoprobes designed for 5 mm NMR tubes, but only 3 mm NMR tubes were
172 used in this project. Protein concentrations were 0.6 mM and 0.2 mM for ^{15}N-HSQC spectra
173 of samples labelled with the C2 and C12 tag, respectively. The protein concentrations were 0.4
174 mM for ^{13}C-HSQC and NOE-relayed ^{13}C-HSQC spectra. ^{15}N-HSQC spectra were recorded at
175 a ^{1}H-NMR frequency of 800 MHz with t_{1max} = 40 ms, t_{2max} = 170 ms, using a total recording
176 time of 3 h per spectrum. ^{13}C-HSQC spectra were recorded with a S^{3}E filter to select the low-
177 field doublet component due to the $^{1}J_{HC}$ coupling of the ^{13}C-labelled tryptophan side chains.
178 The pulse sequence is shown in Fig. S8 and the spectra were recorded at a ^{1}H-NMR frequency
179 of 600 MHz using t_{1max} = 20–50 ms, t_{2max} = 106 ms and total recording times of 2 h per
180 spectrum. ^{13}C-HSQC spectra with NOE relay were recorded without decoupling in the ^{13}C-
181 dimension, relying on relaxation and ^{13}C equilibrium magnetisation to emphasize the narrow
182 doublet component. The NOE mixing time was 150 ms and the total recording time 3 h per
183 spectrum. The pulse sequence is shown in Fig. S9.
184   To account for uncertainties in concentration measurements, samples with L-captopril
185 were prepared with a nominal ratio of captopril to protein of 1.5:1. In the case of samples
186 tagged with the C2 tag, however, this lead to gradual release of some of the tag, as captopril
187 contains a free thiol group and the disulfide linkage of the C2 tag is sensitive to chemical
188 reduction. To limit this mode of sample degradation, the NOE-relayed [^{13}C,^{1}H]-HSQC spectra
189 were recorded with a smaller excess of captopril.
190
191 **2.3 Δχ-tensor fits**
192 The experimental PCSs ($\Delta\delta^{PCS}$) were measured in ppm as the amide proton chemical shift
193 observed in NMR spectra recorded for the IMP-1 mutants A53C, N172C and S204C tagged
194 with Tm^{3+} or Tb^{3+} tags minus the corresponding chemical shift measured of samples made with
195 Y^{3+} tags. The resonance assignments of the wild-type Zn$_2$ enzyme (BMRB entry 25063) were
196 used to assign the ^{15}N-HSQC cross-peaks in the diamagnetic state. The program Paramagpy
197 (Orton et al., 2020) was used to fit magnetic susceptibility anisotropy ($\Delta\chi$) tensors to crystal
198 structures of IMP-1 solved in the absence and presence of the inhibitor captopril.

199

3 Results

3.1 Protein production

Three cysteine mutants of uniformly ^{15}N-labelled IMP-1 were produced *in vivo*, where cysteine residues replaced Ala53, Asn172 and Ser204, respectively. The purified proteins were tagged with C2 tags containing Tb^{3+} or Tm^{3+} as the paramagnetic ions and Y^{3+} as the diamagnetic reference. Samples of the uniformly ^{15}N-labelled mutant N172C were also ligated with C12 tags containing the same set of metal ions. The chemical structures of the tags are depicted in Fig. S1. To record ^{13}C-^{1}H correlation spectra of the tryptophan side chains with minimal spectral overlap, additional samples of the cysteine mutants were produced with selectively ^{13}C-labelled tryptophan residues. These samples were produced by cell-free protein synthesis in the presence of 7-^{13}C indole, deuterated except at the 7 position, with the omission of tryptophan, using a recently established protocol (Maleckis et al., 2021). The residual activity of tryptophan synthase in the cell-free extract was sufficient to produce tryptophan from the added ^{13}C-labelled indole. The resulting tryptophan residues contained a ^{13}C-^{1}H group in position 7 ($^{13}C^{\zeta 2}$ and $^1H^{\zeta 2}$ in IUPAC nomenclature; Markley et al., 1998) and deuterons at all other hydrogen positions of the indole ring except for the H^N atom ($H^{\epsilon 1}$ in IUPAC nomenclature). The cell-free expression yielded about 2 mg of purified protein per millilitre of inner cell-free reaction mixture. Mass spectrometry indicated that the tryptophan residues of IMP-1 were $^{13}C/^2H$-labelled with about 80 % labelling efficiency at each of the six tryptophan positions (Fig. S2). The purified proteins were ligated with C2-Ln^{3+} tags containing either Tb^{3+}, Tm^{3+} or Y^{3+} as in the case of the ^{15}N-labelled samples. Ligation yields with the C2 tags were practically complete as indicated by mass spectrometry (Fig. S2). The ligation yield of the N172C mutant with C12 tags was about 90 % (Herath et al., 2021).

3.2 NMR experiments and resonance assignments

[^{15}N,^{1}H]-HSQC spectra were measured of the tagged proteins in the free state and in the presence of L-captopril (Fig. S3–S7). ^{1}H PCSs of backbone amide protons measured in these spectra were used to establish the $\Delta\chi$ tensors relative to the protein. The resonance assignment of the [^{15}N,^{1}H]-HSQC spectra in the presence of inhibitor was transferred from the corresponding spectra recorded in the absence of inhibitor. As no resonance assignments could reliably be made in this way in areas of spectral overlap, fewer resonance assignments were available in the presence than absence of inhibitor. Furthermore, due to captopril releasing

233 some of the C2 tags from the protein by breaking the disulfide bridge of the tag attachment,

234 spectra recorded in the presence of captopril contained additional cross-peaks from

235 diamagnetic protein.

236 To obtain tagged protein that is inert against chemical reduction, we also attached the

237 C12 tag to the mutant N172C. This tag, however, caused the appearance of additional peaks in

238 the [^{15}N,^{1}H]-HSQC spectra (Fig. S6). The additional peaks appeared in different sample

239 preparations, indicating sample degradation or perturbation of the local protein structure by the

240 tag. We therefore based the rest of the work mainly on the PCSs obtained with the C2 tags.

241 Tables S1 and S2 list the PCSs of the backbone amides measured in the absence and presence

242 of captopril.

243 ^{1}H PCSs of the tryptophan H$^{\zeta 2}$ protons were measured in [^{13}C,^{1}H]-HSQC spectra

244 recorded with S^{3}E spin-state selection element (Meissner et al., 1997) in the ^{13}C dimension to

245 select the slowly relaxing components of the doublets split by $^1J_{HC}$ couplings. Cross-peaks were

246 observed for all six tryptophan residues except for the mutant N172C, which displayed cross-

247 peaks of only five tryptophan indoles (Fig. 2). The missing signal was attributed to Trp176

248 because of its close proximity to the tagging site. The indole H$^{\varepsilon 1}$ proton is located within 2.9 Å

249 of the H$^{\zeta 2}$ proton and the NOE between both protons was readily observed in a [^{13}C,^{1}H]-HSQC

250 experiment with NOE relay (Fig. 2). The H$^{\varepsilon 1}$ chemical shifts afforded better spectral resolution

251 than the H$^{\zeta 2}$ resonances. Comparison of the predicted and observed PCSs yielded resonance

252 assignments of all tryptophan H$^{\varepsilon 1}$ cross-peaks with particular clarity in the NOE-relayed

253 [^{13}C,^{1}H]-HSQC spectrum (Fig. 2). In addition, the assignment was supported by paramagnetic

254 relaxation enhancements (for example, Trp88 is near residue 53 and therefore its cross-peaks

255 were strongly attenuated in the paramagnetic samples of the A53C mutant). Different PCSs

256 were observed for all six tryptophan sidechains and different PCSs were observed for the H$^{\zeta 2}$

257 and H$^{\varepsilon 1}$ protons within the same indole sidechain. Each of the tryptophan sidechains showed

258 PCSs in most, if not all, of the mutants. As the L3 loop is near residue 172, the mutant N172C

259 endowed Trp28 with particularly large PCSs. Tables S3 and S4 report the PCSs measured in

260 this way for the samples labelled with C2 tags.

261 In contrast, assigning the indole N-H groups in the [^{15}N,^{1}H]-HSQC spectra was much

262 more difficult because IMP-1 is a protein prone to showing more than a single peak per proton

263 (Fig. S5). In particular, the [^{15}N,^{1}H]-HSQC spectrum of wild-type IMP-1 selectively labelled

264 with ^{15}N-tryptophan displayed five intense and at least three weak N$^{\varepsilon 1}$–H$^{\varepsilon 1}$ cross-peaks

265 (Carruthers 2014) and the [^{15}N,^{1}H]-HSQC spectra of the tagged cysteine mutants showed

266 evidence of heterogeneity too (Fig. S5). Nonetheless, the five most intense $N^{\varepsilon 1}$–$H^{\varepsilon 1}$ cross-peaks

267 could be assigned by comparison to the PCSs observed in the NOE-relayed [^{13}C,^{1}H]-HSQC

268 spectrum and this assignment was used to measure the PCSs of the tryptophan $H^{\varepsilon 1}$ resonances

269 in the mutant N172C tagged with C12 tag (Fig. S7; Table S4).

270   Spectra recorded in the presence of L-captopril were very similar to those recorded

271 without the inhibitor, except that some new, narrow C-H cross-peaks appeared in the [^{13}C,^{1}H]-

272 HSQC spectra of the mutants A53C and S204C, which were suggestive of protein degradation

273 (Fig. 3). We consequently used the better-resolved indole H^N cross-peaks to identify the correct

274 parent C-H cross-peaks. The chemical shifts of the tryptophan sidechains changed very little

275 in response to the presence of L-captopril, except for the ^{13}C-chemical shift of Trp28, which is

276 nearest to the ligand binding site. The PCSs of the indole protons measured in the presence of

277 the inhibitor are listed in Tables S5 and S6.

278

3.2 Δχ-tensor fits

280 The Δχ-tensor parameters were determined using the program Paramagpy (Orton et al., 2020),

281 using all available ^{1}H PCSs measured of backbone amides. Comparing the Δχ tensor fits to the

282 crystal structures 5EV6 chains A and C (Hinchliffe et al., 2016) and 1DDK (Concha et al.,

283 2000) of the free protein, the chain A of the structure 5EV6 proved to produce the smallest Q

284 factor by a small margin (Fig. S10) and was used as the reference structure of the free protein

285 for the subsequent evaluation. Similarly, chain A of the co-crystal structure published with the

286 inhibitor L-captopril (PDB ID: 4C1F; Brem et al., 2016) on average delivered better fits than

287 chain B and was used as the reference structure for the NMR data recorded in the presence of

288 L-captopril. The Δχ-tensor fits of each mutant and tag used a common metal position for the

289 data obtained with the Tb^{3+} and Tm^{3+} tags. The fits positioned the paramagnetic centres at

290 distances between 8.9 and 10.2 Å from the C$^\alpha$ atom of the tagged cysteine residues, which is

291 compatible with the chemical structure of the C2-tag. Figure 4 shows the correlations between

292 back-calculated and experimental PCSs and Table S7 reports the fitted Δχ tensor parameters.

293 Very similar Q factors were obtained when using the PCSs measured in the absence of inhibitor

294 to fit the Δχ tensor to the co-crystal structure 4C1F or the PCSs measured in the presence of

295 inhibitor to fit the Δχ tensor to the crystal structure of the free protein. This indicates that the

296 protein structure did not change very much in response to inhibitor binding. This conclusion

297 was also indicated by the similarity between the backbone PCSs observed with and without

298 inhibitor (Fig. S11).

299   The $\Delta\chi$ tensors obtained with the Tb^{3+} tags were larger than those obtained with the

300   Tm^{3+} tags, which is also reflected by the consistently larger PCSs observed in the ^{13}C-^{1}H

301   correlation spectra of Fig. 2 and 3. The fits of $\Delta\chi$ tensors to the protein backbone also yielded

302   better Q factors for PCSs generated by Tb^{3+} than Tm^{3+} ions. Therefore, we determined the

303   localization spaces of the tryptophan sidechains in the first instance by using their ^{1}H PCSs

304   measured with Tb^{3+} tags only.

305

306
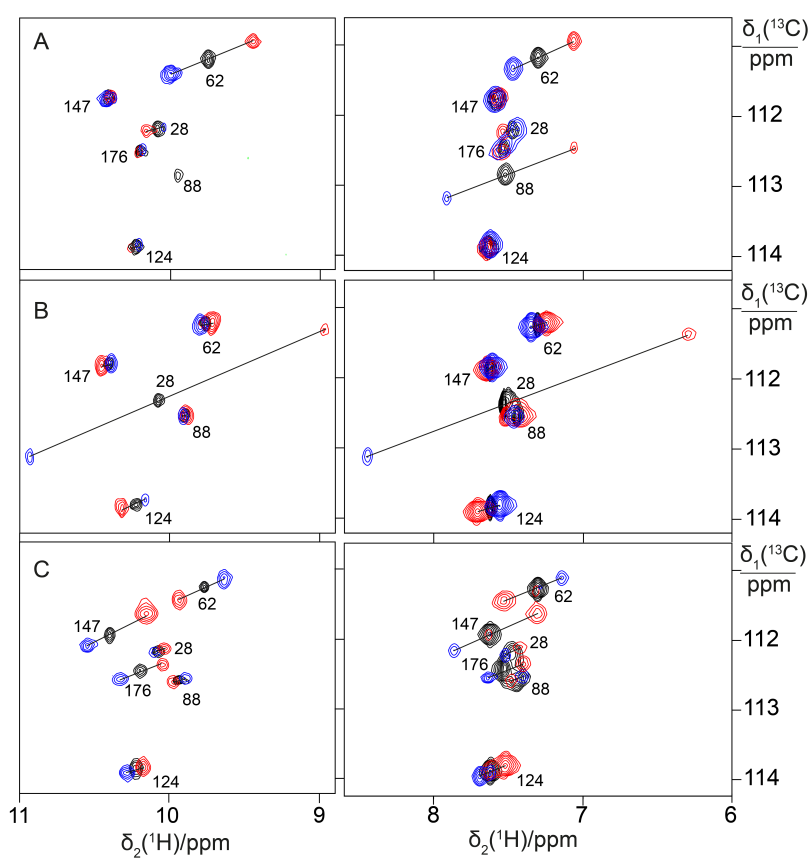
Figure 2. PCSs observed in ^{13}C-^{1}H correlation spectra of 0.4 mM solutions of IMP-1 mutants

labelled with 7-^{13}C-tryptophan (deuterated in the indole positions 2, 4, 5 and 6) and tagged with

C2-Ln^{3+} tags. The plots show superimpositions of spectra recorded with diamagnetic (C2-Y^{3+},

black) or paramagnetic (C2-Tb^{3+}, red; C2-Tm^{3+}, blue) tags. All spectra were recorded with

spin-state selection in the ^{13}C-dimension to record the narrow low-field component of each

312 ^{13}C-doublet. Right panels: [^{13}C,^{1}H]-HSQC spectra. Left panels: [^{13}C,^{1}H]-HSQC spectra with

313 150 ms NOE relay to record the H$^{\varepsilon 1}$ resonances of the tryptophan side chains. PCSs are

314 indicated by lines connecting the peaks of paramagnetic and diamagnetic samples. The cross-

315 peaks are assigned with the residue number of the individual tryptophan residues. (A) Mutant

316 A53C. (B) Mutant N172C. (C) Mutant S204C.
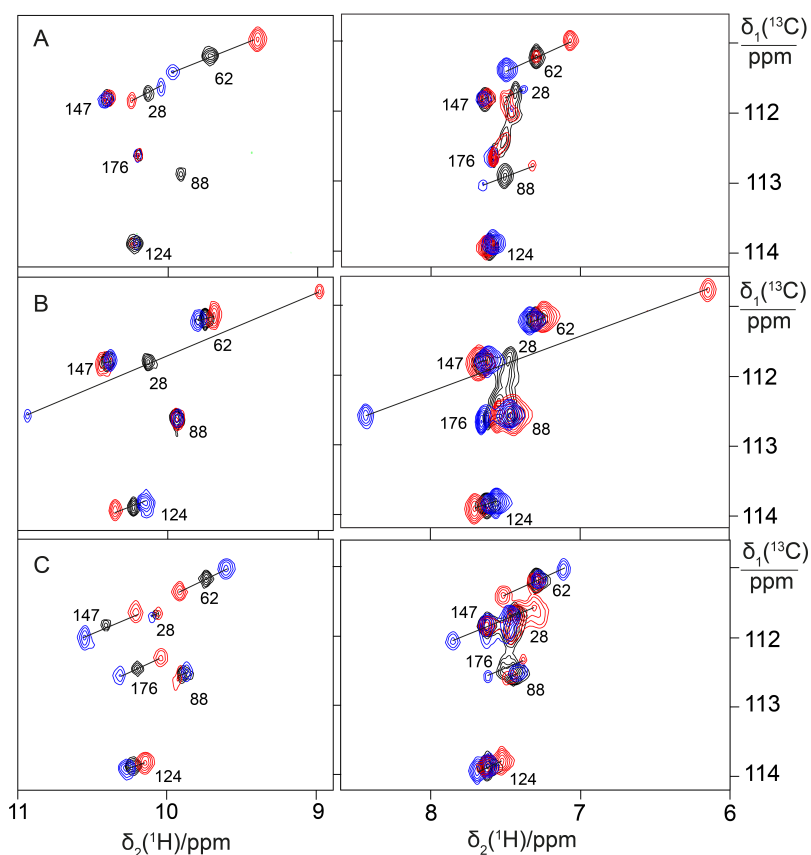
317

318 **Figure 3.** PCSs observed in ^{13}C-^{1}H correlation spectra of 0.4 mM solutions of IMP-1 mutants

319 recorded in the presence of L-captopril. Protein preparations and experimental parameters were

320 the same as in Fig. 2. Spectra recorded with diamagnetic (C2-Y^{3+}, black) or paramagnetic (C2-

321 Tb^{3+}, red; C2-Tm^{3+}, blue) tags are superimposed. Right column: [^{13}C,^{1}H]-HSQC spectra. Left

322 column: [^{13}C,^{1}H]-HSQC spectra with 150 ms NOE. (A) Mutant A53C. (B) Mutant N172C. (C)

323 Mutant S204C.

324
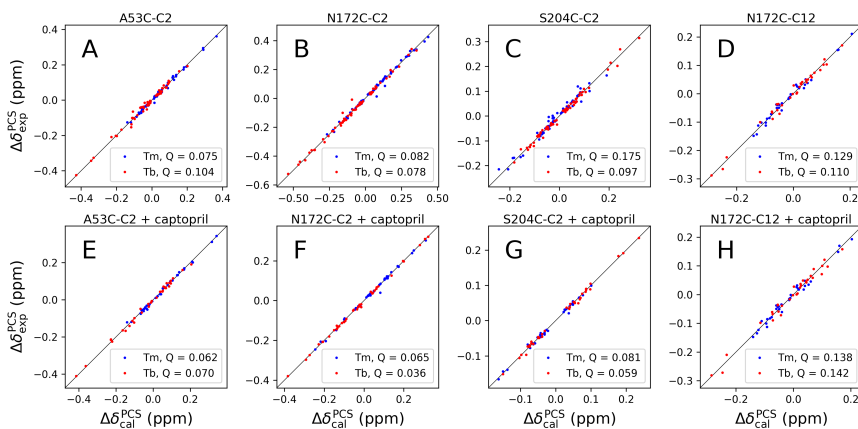
Figure 4. Correlations between back-calculated and experimental ^{1}H PCSs measured of backbone amides of IMP-1 with C2 tags at three different sites (positions 53, 172 and 204) and the C12 tag in position 172. Red and blue data points correspond to the PCS data obtained with Tb^{3+} and Tm^{3+} tags, respectively. (A) Mutant A53C with C2 tag. (B) Mutant N172C with C2 tag. (C) Mutant S204C with C2 tag. (D) Mutant N172C with C12 tag. (E) Same as (A) but in the presence of captopril. (F) Same as (B) but in the presence of captopril. (G) Same as (C) but in the presence of captopril. (H) Same as (D) but in the presence of captopril. PCS data in (A)–(D) were used to fit $\Delta\chi$ tensors to the structure 5EV6. PCS data in (E)–(F) were used to fit $\Delta\chi$ tensors to the structure 4C1F.

3.3 Determining the localisation spaces of tryptophan sidechains

The $\Delta\chi$ tensors determined of backbone amides not only enabled the resonance assignment of the tryptophan sidechains by comparing back-calculated with experimental PCSs, but also allowed translation of the indole PCSs into restraints that define the locations of the tryptophan H$^{\zeta 2}$ and H$^{\varepsilon 1}$ atoms with respect to the rest of the protein. The concept of localising nuclear spins by PCSs that are generated by lanthanoid tags at different sites is well-established (see, e.g., Yagi et al., 2013; Lescanne et al., 2018; Zimmermann et al., 2019). It can be visualised by representing each PCS restraint by the corresponding PCS isosurface, which comprises all points in space where this PCS value is generated by the $\Delta\chi$ tensor (Fig. 5). With PCS restraints from two different metal sites, the intersection between the respective isosurfaces defines a line. The intersection of this line with the PCS isosurface from a third $\Delta\chi$ tensor defines two points. While a fourth $\Delta\chi$ tensor could unambiguously produce a single solution, a fourth tensor

351 may not be required if one of these two points is incompatible with the covalent structure of
352 the protein. In favourable circumstances, the constraints imposed by the covalent structure may
353 even allow the accurate positioning of nuclear spins by PCSs generated from only two different
354 $\Delta\chi$ tensors (Pearce et al., 2017). Therefore, the present study was successful with only three
355 different tagging sites. Figure S12 illustrates the concept for the Trp28 $H^{\epsilon 1}$ atom.

356 The spatial definition of the intersection point defined by the PCS isosurfaces depends
357 on the experimental uncertainties in a non-isotropic way, as the PCS isosurfaces rarely intersect
358 in an orthogonal manner and the PCS gradients differ for each $\Delta\chi$ tensor. To capture a
359 localisation space, which allows for the experimental uncertainty in the measured PCS data,
360 we mapped the spatial field of root-mean-squared deviations (RMSD) between experimental
361 and calculated PCS values and defined the boundary of the localisation space by a maximal
362 RMSD value. In addition, uncertainties in the $\Delta\chi$ tensors were propagated by averaging over
363 the results from 20 $\Delta\chi$-tensor fits performed with random omission of 20 % of the backbone
364 PCS data. In the present work, the routine for defining the localisation space was implemented
365 as a script in the software Paramagpy (Orton et al., 2020). Figure 6 shows the resulting
366 localisation spaces for the $H^{\epsilon 1}$ and $H^{\zeta 2}$ atoms of Trp28, using the PCS data obtained for the
367 three cysteine mutants A53C, N172C and S204C with the C2-Tb^{3+} tag as well as the N172C
368 mutant with the C12-Tb^{3+} tag.

369 The localisation spaces found for the $H^{\epsilon 1}$ and $H^{\zeta 2}$ atoms of Trp28 were clearly different.
370 Furthermore, the distance between them corresponded closely to the distance expected from
371 the chemical structure of the indole ring (2.9 Å). The irregular shapes of the localisation spaces
372 displayed in Fig. 5 purely reflect the relative geometry of the intersecting PCS isosurfaces and
373 do not take into account any dynamic flexibility of the L3 loop or protein structure. In
374 particular, the relevant PCS isosurfaces associated with the C2 tag at sites N172C and S204C
375 intersect at a shallow angle, which leads to the elongated shape of the localisation space for the
376 Trp28 $H^{\zeta 2}$ atom (Fig. S12). For the nitrogen-bound $H^{\epsilon 1}$ atom, the localisation space was
377 restricted further by the additional data obtained with the C12 tag at site N172C (Fig. 6).
378 Calculating the localisation spaces from the Tm^{3+} data yielded very similar results (Fig. S13).
379 The agreement of the localisation spaces of Trp28 with chain A of the previously published
380 crystal structure 5EV6 is excellent and they are clearly incompatible with the conformations
381 observed in chain C of the same structure or in the structure 1DDK (Fig. 1).

382 Due to close proximity to the C2 tags in the N172C mutant, the largest PCSs were
383 observed for Trp28 $H^{\epsilon 1}$ but, in the absence of captopril, their exact magnitude appeared about

384 0.3 ppm smaller in the [^{15}N,^{1}H]-HSQC (Fig. S5b) than the NOE-relayed [^{13}C,^{1}H]-HSQC (Fig.

385 2B) spectrum. The centre of the localisation space of Trp28 H$^{\epsilon 1}$ moved to a slightly more open

386 L3 loop conformation when using the smaller PCS detected in the [^{15}N,^{1}H]-HSQC spectrum

387 of the N172C mutant labelled with the C2-Tb^{3+} tag. The space still encompassed the

388 coordinates observed in the structure 5EV6, limiting the significance of this difference in PCS.

389

390 **3.4 Defining the localisation space with one versus two lanthanoid ions in the same tag**

391 **and at the same site**

392 Unexpectedly, determining separate localisation spaces from the Tm^{3+} and Tb^{3+} datasets

393 yielded more plausible results than when both datasets were used simultaneously. Careful

394 inspection showed that the close alignment of the $\Delta\chi$ tensors of the Tm^{3+} and Tb^{3+} data resulted

395 in particularly shallow intersection angles of the respective PCS isosurfaces. In calculating the

396 localisation space of Trp28, the PCS isosurfaces arising from the N172C mutant carried by far

397 the greatest weight as this site is closer to residue 28 than the sites 53 and 204. Therefore, the

398 Tm^{3+} and Tb^{3+} data from the N172C mutant dominated the PCS RMSD calculation and the

399 intersection between the associated isosurfaces pulled the final localisation space to a

400 structurally implausible location, which was unstable with respect to small perturbations in $\Delta\chi$-

401 tensor orientations associated with the tensors at site 172. In contrast, considering the Tm^{3+} and

402 Tb^{3+} datasets separately allowed the localisation spaces to be determined by the intersections

403 with PCS isosurfaces from the other sites. The resulting localisation spaces consistently were

404 compatible with crystal structures.

405
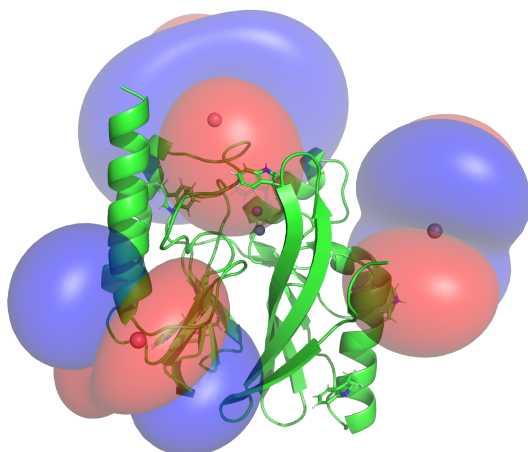
406

407 **Figure 5.** PCS isosurfaces of the IMP-1 mutants A53C, N172C and S204C plotted on the
408 crystal structure 5EV6. The respective Δχ tensors were determined from the ^{1}H PCSs measured
409 of backbone amides. Blue/red isosurfaces correspond to PCSs of +/-1.0 ppm, respectively,
410 generated with C2-Tb^{3+} tags.

411

412
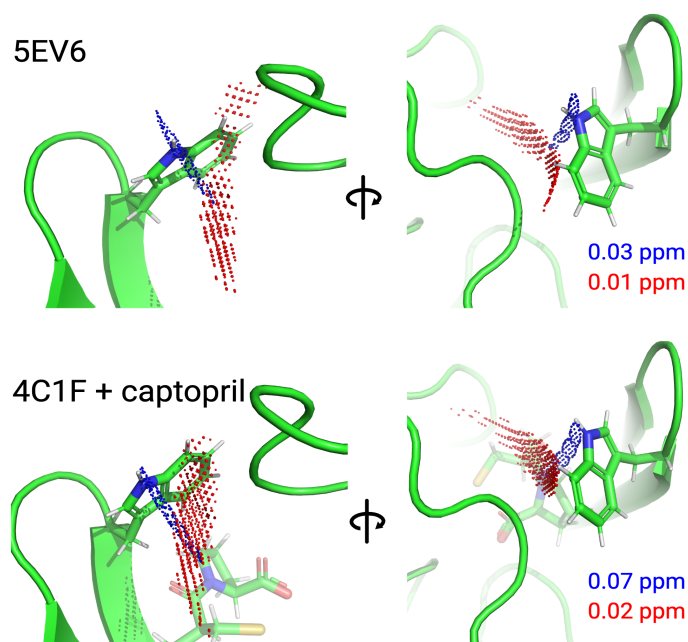
413

414 **Figure 6.** Localisation space of the sidechain of Trp28 defined by the PCSs from tags in the
415 IMP-1 mutants A53C, N172C and S204C. Red and blue points outline localisation spaces
416 determined for the H^{ζ2} and H^{ε1} atoms, respectively. The localisation space of the H^{ζ2} atom was
417 defined by the PCSs and Δχ tensors determined for the Tb^{3+}-loaded C2 tags, while the
418 localisation space of the H^{ε1} atom was restricted by additional data obtained with C12-Tb^{3+} tag
419 at site N172C. The boundaries of the respective localisation spaces displayed are defined by
420 the PCS RMSD values indicated in ppm. The top panel depicts the localisation spaces
421 determined for the free protein plotted on chain A of the crystal structure 5EV6 depicted in two
422 different orientations. The lower panel depicts the localisation spaces determined in the
423 presence of captopril plotted on chain A of the crystal structure 4C1F.

424

3.5 L3 loop conformation in the presence of L-captopril

425

426   Figure 6 shows that, within the uncertainty of the experiments, the localisation space of the

427   indole sidechain of Trp28 is invariant with respect to the presence or absence of captopril.

428   Conservation of the L3 loop conformation with and without inhibitor is supported by the close

429   similarity in all the PCSs observed for Trp28 in the NOE-relayed [^{13}C,^{1}H]-HSQC spectra (Fig.

430   2 and 3). In the [^{1}H,^{15}N]-HSQC spectra of the mutant N172C with C2 tag, however, the PCSs

431   observed for Trp28 H$^{\epsilon 1}$ appeared somewhat smaller without than with captopril (Fig. S5b). As

432   the PCSs of backbone amides were very similar in the absence and presence of the inhibitor

433   (Fig. S11), this difference in PCS suggests a change in L3 loop conformation that did not arise

434   in the selectively ^{13}C-labelled samples. As discussed above, using the smaller PCS of Trp28

435   H$^{\epsilon 1}$ did not sufficiently change its localisation space in the free protein to render it incompatible

436   with the coordinates of the structure 5EV6. We therefore have little evidence for a significant

437   conformational change of the L3 loop between the free and bound state.

438   The cross-peak intensities of the Trp28 sidechain resonances are relatively weak

439   compared with those of the other tryptophan sidechains, suggesting that Trp28 is subject to

440   dynamics that broaden its resonances. Its cross-peaks appeared slightly weaker in the presence

441   than in the absence of inhibitor (Fig. 2 and 3), suggesting a change in dynamics caused by the

442   inhibitor binding. Previous NMR studies of metallo-β-lactamases reported faster R_2(^{15}N)

443   relaxation rates of the L3-loop tryptophan sidechain in the presence than in the absence of

444   inhibitor, which was attributed to dampened dynamics (Huntley et al., 2000; Softley et al.,

445   2020). In the presence of dynamics, the localisation spaces determined in the present work

446   must be considered averages that do not report on the amplitude or direction of motions.

447

3.6 Localisation spaces of tryptophan side chains other than Trp28

448

449   As the tagging sites had been designed to analyse the conformation of the L3 loop, they were

450   positioned at similar distances from the L3 loop and therefore not optimal for determining

451   localisation spaces of the other tryptophan residues. Nonetheless, clear differences were

452   observed in the PCSs of the H$^{\xi 2}$ and H$^{\epsilon 1}$ atoms (Fig. 2), allowing the separation of the respective

453   localisation spaces, which also proved to be in excellent agreement with the conformations of

454   the side-chain indoles of Trp62, Trp124 and Trp147 as found in the crystal structure (Fig. S14),

455   whereas the data were insufficient to determine the sidechain conformation of Trp176.

456

4 Discussion

457

458   The L3 loop of metallo-β-lactamases is known to be flexible and, in the specific case of IMP-

459   1, significantly assists in substrate binding and enzymatic activity (Moali et al., 2003). As the

460   substrate is sandwiched between the di-zinc site and the L3 loop, it is tempting to think that the

461   loop opens up for substrate binding and product release while it may be closed during the

462   enzymatic reaction to hold the substrate and reaction intermediate in place. In contrast, some

463   of the conformations observed in crystal structures of IMP-1 obtained in the presence and

464   absence of the inhibitor L-captopril, revealed the loop in almost identical conformations (Brem

465   et al., 2016). This observation is inconclusive, however, as the L3 loop forms more extensive

466   intermolecular contacts with neighbouring protein molecules in the crystal lattice than

467   intramolecular contacts. In addition, other crystal structures observed the loop to move by

468   almost 3 Å in response to a different inhibitor (Concha et al., 2000). This prompted us to probe

469   its actual location in the absence of crystal packing forces in solution, a task which is difficult

470   to tackle by traditional NMR spectroscopic methods that rely on short-range NOEs.

471   Our results show that by furnishing IMP-1 with paramagnetic lanthanoid tags, the

472   coordinates of the indole sidechain of Trp28, which is a key residue near the tip of the loop,

473   can be determined with remarkable accuracy even in the free protein, where the available

474   crystal structures position the L3 loop in a conformation without any direct contacts with the

475   core of the protein. Indeed, the localisation space identified by the NMR data of the free protein

476   proved to be sufficiently well-defined to discriminate between different crystal structures of

477   IMP-1, as well as between different chains in the same asymmetric crystal unit. For example,

478   the sidechain orientation of Trp28 observed in $[Fe^{3+},Zn^{2+}]$-IMP-1 (4UAM; Carruthers et al.,

479   2014) proved to be in poor agreement with the PCS data, whereas the data were in full

480   agreement with chain A in the structure 5EV6 of $[Zn^{2+},Zn^{2+}]$-IMP-1 without inhibitor

481   (Hinchliffe et al., 2016) and chain A in the structure 4C1F with bound L-captopril (Brem et al.,

482   2016). This highlights the outstanding capacity of PCSs to assess small conformational

483   differences.

484   The approach of using PCSs for local structure determination is particularly appealing

485   in the case of difficult proteins such as IMP-1, where the sequence-specific NMR resonance

486   assignments are incomplete due to line-broadening attributable to motions in the μs–ms time

487   range and additional signals are observed that either stem from protein degradation, misfolding

488   or alternative conformations in slow exchange with the main structure. Notably, all information

489   required to establish the Δχ tensors could be obtained from resolved cross-peaks observed in

490   sensitive $[^{15}N,^{1}H]$-HSQC spectra. Similarly, the localisation information of the tryptophan

491 sidechains could be obtained from sensitive ^{13}C-^{1}H and ^{15}N-^{1}H correlation spectra. Positioning

492 the lanthanoid tags relatively far from the substrate binding site avoided direct interference

493 with the binding loop structure.

494   In the face of additional signals from minor species, site-selective ^{13}C-labelling of the

495 tryptophan sidechains was particularly helpful for simplifying the [^{13}C,^{1}H]-HSQC spectra.

496 Gratifyingly, this could be achieved by providing suitably labelled indole without having to

497 synthesise the full amino acid (Maleckis et al., 2021).

498   It has been pointed out previously that the accuracy with which localisation spaces can

499 be determined is best when PCS isosurfaces intersect in an orthogonal manner (Pintacuda et

500 al., 2006; Lescanne et al., 2018; Zimmermann et al., 2019). In the present work, we found that,

501 counterintuitively, the provision of additional data can considerably degrade the accuracy of

502 the localisation space. This effect arises when PCS isosurfaces intersect at a shallow angle, as

503 the location of these intersections becomes very sensitive with regard to small errors in the

504 relative orientations of the underpinning $\Delta\chi$ tensors. Shallow intersection angles of PCS

505 isosurfaces are common, when two PCS datasets are from tags and tagging sites that differ only

506 in the identity of the paramagnetic metal ion in the tag. This situation commonly generates $\Delta\chi$

507 tensors of different magnitude and sign, but closely similar orientation (Bertini et al., 2001; Su

508 et al., 2008; Keizers et al., 2008; Man et al., 2010; Graham et al., 2011; Joss et al., 2018;

509 Zimmermann et al., 2021). Therefore, while the use of Tm^{3+} and Tb^{3+} tags is helpful for

510 assigning the cross-peaks in the paramagnetic state, more robust results are obtained by using

511 only one of these data sets for calculating the localisation space. Good localisation spaces were

512 thus obtained by using only PCSs measured for Tb^{3+} tags (Fig. 6) or only PCSs measured for

513 Tm^{3+} tags (Fig. S12). In contrast, however, very different tags attached at the same site, such

514 as the C2 and C12 tags installed in the mutant N172C, produced independent $\Delta\chi$-tensor

515 orientations and therefore contributed positively to localising the Trp28 $H^{\epsilon1}$ atom.

516   In principle it is inappropriate to explain a set of PCSs by a single $\Delta\chi$ tensor, if they are

517 generated by a lanthanoid tag attached via a flexible linker, which positions the lanthanide ions

518 at variable coordinates relative to the protein. In this situation, fitting a single $\Delta\chi$ tensor

519 amounts to an approximation. The effective $\Delta\chi$ tensors obtained in this way, however, can

520 fulfill the PCSs remarkably well (Shishmarev and Otting, 2013), as illustrated by the low Q

521 factors obtained in this work (Fig. 4), and the localisation spaces obtained for the tryptophan

522 sidechains are correspondingly well defined.

523   The present work employed ^{1}H PCSs only, although PCSs were also observed in the

indirect dimensions of the [^{13}C,^{1}H]-HSQC and [^{15}N,^{1}H]-HSQC spectra. We made this choice because the paramagnetic tags give rise to weak molecular alignments in the magnetic field, which result in residual anisotropic chemical shifts (RACS). The effect is unimportant for ^{1}H spins but significant for nuclear spins with large chemical shift anisotropy (CSA) tensors such as backbone nitrogens and aromatic carbons. Correcting for the RACS effect is possible with prior knowledge of the CSA tensors and bond orientations (John et al., 2005). We therefore chose not to measure PCSs of the heteronuclear spins in favour of improving sensitivity by accepting a lower spectral resolution in the indirect dimensions.

Finally, the C12 tag was designed specifically with the intent to produce a more rigid tether to the protein than the C2 tag, but this did not result in larger $\Delta\chi$ tensors (Table S7) and the NMR spectra of IMP-1 N172C displayed more heterogeneity with the C12 than the C2 tag, suggesting that the shorter and more rigid tether combined with the fairly high molecular weight of the cyclen-lanthanoid complex may have perturbed the protein structure to some degree.

5 Conclusion

The current work illustrates how $\Delta\chi$ tensors from paramagnetic lanthanoid ion tags installed at three different sites of the protein can be used to probe the conformation of a selected site in solution in unprecedented detail, provided the structure of most of the protein is known with high accuracy to allow fitting effective $\Delta\chi$ tensors of high predictive value. Importantly, however, the method is easily compromised, if two PCS isosurfaces intersect at a shallow angle as, in this situation, inaccuracies in $\Delta\chi$ tensor determinations have an outsized effect on positioning the localisation spaces defined by the PCSs. Therefore, improved results were obtained by not combining data from different metal ions bound to otherwise identical tags and tagging sites. In the present work, simplifying the NMR spectrum of tryptophan residues by site-selective isotope labelling proved to be of great value for sufficiently improving the spectral resolution to allow assigning the labelled resonances solely from PCSs and PREs. The strategy opens a path to detailed structural investigations of proteins of limited stability like IMP-1, for which complete assignments of the NMR spectrum are difficult to obtain.

Code and data availability. NMR spectra and pulse programs are available at https://doi.org/10.5281/zenodo.5518294. The script for calculating localisation spaces is available at https://doi.org/10.5281/zenodo.3594568 and from the GitHub site of Paramagpy.

585

Supplement. The supplement related to this article is available online at: https://doi.org/...

587

Author contributions. GO initiated the project and edited the final version of the manuscript. HWO wrote NMR pulse programs and software to calculate localisation spaces and performed the $\Delta\chi$ tensor and structure analysis. IDH made labelled protein samples, recorded and assigned NMR spectra, measured PCSs and wrote the first version of the manuscript. AM synthesised the isotope-labelled indole. SJ made ^{15}N-labelled protein mutants with C2 tags and assigned PCSs of backbone amides. MS synthesized C2 tags with different lanthanoid ions. CB, LT and SB synthesized C12 tags with different lanthanoid ions.

595

Competing interests. The authors declare that they have no conflict of interest.

597

Financial support. GO thanks the Australian Research Council for a Laureate Fellowship (grant no. FL170100019) and project funding through the Centre of Excellence for Innovations in Peptide and Protein Science, Australian Research Council (grant no. CE200100012). AM thanks the European Regional Development Fund (ERDF) for funding (PostDoc project No. 1.1.1.2/VIAA/2/18/381).

References

Arakawa, Y., Murakami, M., Suzuki, K., Ito, H., Wacharotayankun, R., Ohsuka, S., Kato, N., and Ohta, M.: A novel integron-like element carrying the metallo-β-lactamase gene bla_{IMP}, Antimicrob. Agents Chemother., 39, 1612–1615, https://doi.org/10.1128/AAC.39.7.1612, 1995.

Bertini, I., Janik, M. B. L., Lee, Y. M., Luchinat, C., and Rosato, A.: Magnetic susceptibility tensor anisotropies for a lanthanide ion series in a fixed protein matrix, J. Am. Chem. Soc., 123, 4181–4188, https://doi.org/10.1021/ja0028626, 2001.

Brem, J., van Berkel, S. S., Zollman, D., Lee, S. Y., Gileadi, O., McHugh, P. J., Walsh, T. R., McDonough, M.A., and Schofield, C. J.: Structural basis of metallo-β-lactamase inhibition by captopril stereoisomers, Antimicrob. Agents Chemother., 60, 142–150, https://doi.org/10.1128/AAC.01335-15, 2016.

Brewer, K. D., Bacaj, T., Cavalli, A., Camilloni, C., Swarbrick, J. D., Liu, J., Zhou, A., Zhou, P., Barlow, N., Xu, J., Seven, A. B., Prinslow, E. A., Voleti, R., Häussinger, D., Bonvin, A. M. J. J., Tomchick, D. R., Vendruscolo, M., Graham, B., Südhof, T. C., and Rizo, J.:

Dynamic binding mode of a synaptotagmin-1-SNARE complex in solution, Nat. Struct. Mol. Biol., 22, 555–564, https://doi.org/10.1038/nsmb.3035, 2015.

Bush, K.: Proliferation and significance of clinically relevant β-lactamases, Ann. N. Y. Acad. Sci., 1277, 84−90, https://doi.org/10.1111/nyas.12023, 2013.

Bush, K.: Alarming β-lactamase-mediated resistance in multidrug-resistant *Enterobacteriaceae*, Curr. Opin. Microbiol., 13, 558−564, https://doi.org/10.1016/j.mib.2010.09.006, 2010.

Carruthers, T. J.: Paramagnetism & Structural Biology: Biochemical & Biophysical Analysis of IMP-1 Metallo-β-lactamase, PhD thesis, The Australian National University, Canberra, 221 pp., 2014.

Carruthers, T. J., Carr, P. D., Loh, C.-T., Jackson, C. J., and Otting, G.: Fe^{3+} located in the dinuclear metallo-β-lactamase IMP-1 by pseudocontact shifts. Angew. Chemie Int. Ed., 53, 14269−14272, https://doi.org/10.1002/anie.201408693, 2014.

Chen, W.-N., Nitsche, C., Pilla, K. B., Graham, B., Huber, T., Klein, C. D., and Otting, G.: Sensitive NMR approach for determining the binding mode of tightly binding ligand molecules to protein targets, J. Am. Chem. Soc., 138, 4539−4546, https://doi.org/10.1021/jacs.6b00416, 2016.

Concha, N. O., Rasmussen, B. A., Bush, K., and Herzberg, O.: Crystal structure of the wide-spectrum binuclear zinc β-lactamase from *Bacteroides fragilis*, Structure, 4, 823–836, https://doi.org/10.1016/S0969-2126(96)00089-5, 1996.

Concha, N. O., Janson, C. A., Rowling, P., Pearson, S., Cheever, C. A., Clarke, B. P., Lewis, C., Galleni, M., Frere, J.-M., Payne, D. J., Bateson, J. H., and Abdel-Meguid, S. S.: Crystal Structure of the IMP-1 metallo-β-lactamase from *Pseudomonas aeruginosa* and its complex with a mercaptocarboxylate inhibitor: binding determinants of a potent, broad-spectrum inhibitor, Biochemistry, 39, 4288–4298, https://doi.org/10.1021/bi992569m, 2000.

Crick, D. J., Wang, J. X., Graham, B., Swarbrick, J. D., Mott, H. R., and Nietlispach, D.: Integral membrane protein structure determination using pseudocontact shifts, J. Biomol. NMR, 61, 197–207, https://doi.org/10.1007/s10858-015-9899-6, 2015.

de la Cruz, L., Nguyen, T.H.D., Ozawa, K., Shin, J., Graham, B., Huber, T., and Otting, G.: Binding of low-molecular weight inhibitors promotes large conformational changes in the dengue virus NS2B-NS3 protease: fold analysis by pseudocontact shifts, J. Am. Chem. Soc., 133, 19205–19215, https://doi.org/10.1021/ja208435s, 2011.

Galleni, M., Lamotte-Brasseur, J., Rossolini, G. M., Spencer, J., Dideberg, O., Frère, J.-M., and The Metallo-β-Lactamase Working Group: Standard numbering scheme for class B β-lactamases. Antimicrob. Agents Chemother., 45, 660–663, https://doi.org/10.1128/AAC.45.3.660-663.2001, 2001.

Gianquinto, E., Tondi, D., D'Arrigo, G., Lazzarato, L., and Spyrakis, F.: Can we exploit β-lactamases intrinsic dynamics for designing more effective inhibitors? Antibiotics, 9, 833, https://doi.org/10.3390/antibiotics9110833, 2020.

González, M. M., Abriata, L. A., Tomatis, P. E., and Vila, A. J.: Optimization of conformational dynamics in an epistatic evolutionary trajectory, Mol. Biol. Evol., 33, 1768–1776, https://doi.org/10.1093/molbev/msw052, 2016.

Graham, B., Loh, C.T., Swarbrick, J.D., Ung, P., Shin, J., Yagi, H., Jia, X., Chhabra, S., Pintacuda, G., Huber, T., and Otting, G.: A DOTA-amide lanthanide tag for reliable generation of pseudocontact shifts in protein NMR spectra, Bioconjugate Chem., 22, 2118–2125, https://doi.org/10.1021/bc200353c, 2011.

Guan, J. Y., Keizers, P. H. J., Liu, W. M., Löhr, F., Skinner, S. P., Heeneman, E. A., Schwalbe, H., Ubbink, M., and Siegal, G.: Small-molecule binding sites on proteins established by paramagnetic NMR spectroscopy. J. Am. Chem. Soc., 135, 5859–5868, https://doi.org/10.1021/ja401323m, 2013.

Herath, I. D., Breen, C., Hewitt, S. H., Berki, T. R., Kassir, A. F., Dodson, C., Judd, M., Jabar, S., Cox, N., Otting, G., and Butler, S. J.: A chiral lanthanide tag for stable and rigid attachment to single cysteine residues in proteins for NMR, EPR and time-resolved luminescence studies, Chem. Eur. J., 27, 13009–13023, https://doi.org/10.1002/chem.202101143, 2021.

Hinchliffe, P., González, M. M., Mojica, M. F., González, J. M., Castillo, V., Saiz, C., Kosmopoulou, M., Tooke, C. L., Llarrull, L. I., Mahler, G., and Bonomo, R. A.: Cross-class metallo-β-lactamase inhibition by bisthiazolidines reveals multiple binding modes, Proc. Nat. Acad. Sci., 113, E3745–E3754, https://doi.org/10.1073/pnas.1601368113, 2016.

Hinchliffe, P., Tanner, C. A., Krismanich, A. P., Labbé, G., Goodfellow, V. J., Marrone, L., Desoky, A. Y., Calvopiña, K., Whittle, E. E., Zeng, F., and Avison, M. B.: Structural and kinetic studies of the potent inhibition of metallo-β-lactamases by 6-phosphonomethylpyridine-2-carboxylates, Biochemistry, 57, 1880–1892, https://doi.org/10.1021/acs.biochem.7b01299, 2018.

Hiraiwa, Y., Saito, J., Watanabe, T., Yamada, M., Morinaka, A., Fukushima, T., and Kudo, T.: X-ray crystallographic analysis of IMP-1 metallo-β-lactamase complexed with a 3-aminophthalic acid derivative, structure-based drug design, and synthesis of 3,6-disubstituted phthalic acid derivative inhibitors, Bioorg. Med. Chem. Lett., 24, 4891–4894, https://doi.org/10.1016/j.bmcl.2014.08.039, 2014.

Huntley, J.J.A., Scrofani, S.D.B., Osborne, M.J., Wright, P.E., and Dyson, H.J.: Dynamics of the metallo-β-lactamase from *Bacteroides fragilis* in the presence and absence of a tight-binding inhibitor, Biochemistry, 39, 13356–13364, https://doi.org/10.1021/bi001210r, 2000.

Huntley, J. J. A., Fast, W., Benkovic, S. J., Wright, P. E., and Dyson, H. J.: Role of a solvent-exposed tryptophan in the recognition and binding of antibiotic substrates for a metallo-β-lactamase, Protein Sci., 12, 1368–1375, https://doi.org/10.1110/ps.0305303, 2003.

Ito, H., Arakawa, Y., Ohsuka, S., Wachorotayankun, R., Kato, N., and Ohta, M.: Plasmid-mediated dissemination of the metallo-β-lactamase gene *bla*IMP among clinically isolated strains of *Serratia marcescens*, Antimicrob. Agents Chemother., 39, 824–829, https://doi.org/10.1128/AAC.39.4.824, 1995.

John, M., Park, A. Y., Pintacuda, G., Dixon, N. E., and Otting, G.: Weak alignment of paramagnetic proteins warrants correction for residual CSA effects in measurements of pseudocontact shifts, J. Am. Chem. Soc., 127, 17190–17191, https://doi.org/10.1021/ja0564259, 2005.

John, M., Park, A. Y., Pintacuda, G., Dixon, N. E., and Otting, G.: Weak alignment of paramagnetic proteins warrants correction for residual CSA effects in measurements of pseudocontact shifts, J. Am. Chem. Soc., 127, 17190–17191, https://doi.org/10.1021/ja0564259, 2005.

Joss, D., Walliser, R. M., Zimmermann, K., and Häussinger, D.: Conformationally locked lanthanide chelating tags for convenient pseudocontact shift protein nuclear magnetic resonance spectroscopy, J. Biomol. NMR, 72, 29–38, https://doi.org/10.1007/s10858-018-0203-4, 2018.

Keizers, P. H. J., Saragliadis, A., Hiruma, Y., Overhand, M., and Ubbink, M.: Design, synthesis, and evaluation of a lanthanide chelating protein probe: CLaNP-5 yields predictable paramagnetic effects independent of environment, J. Am. Chem. Soc., 130, 14802–14812, https://doi.org/10.1021/ja8054832, 2008.

Keizers, P. H. J., Mersinli, B., Reinle, W., Donauer, J., Hiruma, Y., Hannemann, F., Overhand, M., Bernhardt, R., and Ubbink, M.: A solution model of the complex formed by adrenodoxin and adrenodoxin reductase determined by paramagnetic NMR spectroscopy, Biochemistry, 49, 6846–6855, https://doi.org/10.1021/bi100598f, 2010.

Kobashigawa, Y., Saio, T., Ushio, M., Sekiguchi, M., Yokochi, M., Ogura, K., and Inagaki, F.: Convenient method for resolving degeneracies due to symmetry of the magnetic susceptibility tensor and its application to pseudo contact shift-based protein-protein complex structure determination, J. Biomol. NMR, 53, 53–63, https://doi.org/10.1007/s10858-012-9623-8, 2012.

Laraki, N., Galleni, M., Thamm, I., Riccio, M. L., Amicosante, G., Frère, J.-M., and Rossolini, G. M.: Structure of In101, a *bla*$_{IMP}$-containing *Pseudomonas aeruginosa* integron phyletically related to In5, which carries an unusual array of gene cassettes, Antimicrob. Agents Chemother., 43, 890–901, https://doi.org/10.1128/AAC.43.4.890, 1999a.

Laraki, N., Franceschini, N., Rossolini, G. M., Santucci, P., Meunier, C., De Pauw, E., Amicosante, G., Frère, J.-M., and Galleni, M.: Biochemical characterization of the *Pseudomonas aeruginosa* 101/1477 metallo-β-lactamase IMP-1 produced by *Escherichia coli*, Antimicrob. Agents Chemother., 43, 902–906, https://doi.org/10.1128/AAC.43.4.902, 1999b.

Lescanne, M., Ahuja, P., Blok, A., Timmer, M., Akerud, T., and Ubbink, M.: Methyl group reorientation under ligand binding probed by pseudocontact shifts, J. Biomol. NMR, 71, 275–285, https://doi.org/10.1007/s10858-018-0190-5, 2018.

Linciano, P., Cendron, L., Gianquinto, E., Spyrakis, F., and Tondi, D.: Ten years with New Delhi metallo-β-lactamase-1 (NDM-1): from structural insights to inhibitor design, ACS Infect. Dis. 5, 9–34, https://doi.org/10.1021/acsinfecdis.8b00247, 2018.

Maleckis, A., Herath, I. D., and Otting, G.: Synthesis of ^{13}C/^{19}F/^{2}H labeled indoles for use as tryptophan precursors for protein NMR spectroscopy, Org. Biomol. Chem., 19, 5133–5147, https://doi.org/10.1039/D1OB00611H, 2021.

Man, B., Su, X.-C., Liang, H., Simonsen, S., Huber, T., Messerle, B. A., and Otting, G.: 3-Mercapto-2,6-pyridinedicarboxylic acid, a small lanthanide-binding tag for protein studies by NMR spectroscopy, Chem. Eur. J., 16, 3827–3832, https://doi.org/10.1002/chem.200902904, 2010.

Markley, J. L., Bax, A., Arata, Y., Hilbers, C. W., Kaptein, R., Sykes, B. D., Wright, P. E., and Wüthrich, K.: Recommendations for the presentation of NMR structures of proteins and

747   nucleic acids - IUPAC-IUBMB-IUPAB Inter-Union Task Group on the Standardization of
748   Data Bases of Protein and Nucleic Acid Structures Determined by NMR Spectroscopy, J.
749   Biomol. NMR, 12, 1–23, https://doi.org/10.1023/A:1008290618449, 1998.

750   Meissner, A., Duus, J. Ø., and Sørensen, O. W.: Spin-state-selective excitation. Application for
751   E.COSY-type measurement of J_{HH} coupling constants, J. Magn. Reson., 128, 92–97,
752   https://doi.org/10.1006/jmre.1997.1213, 1997.

753   Moali, C., Anne, C., Lamotte-Brasseur, J., Groslambert, S., Devreese, B., Van Beeumen, J.,
754   Galleni, M., and Frère, J.M.: Analysis of the importance of the metallo-β-lactamase active
755   site loop in substrate binding and catalysis, Chemistry & Biology, 10, 319–329,
756   https://doi.org/10.1016/S1074-5521(03)00070-X, 2003.

757   Orton, H. W., Huber, T., and Otting, G.: Paramagpy: software for fitting magnetic
758   susceptibility tensors using paramagnetic effects measured in NMR spectra, Magn.
759   Reson., 1, 1–12, https://doi.org/10.5194/mr-1-1-2020, 2020.

760   Palacios, A. R, Mojica, M. F., Giannini, E., Taracila, M. A., Bethel, C. R., Alzari, P. M., Otero,
761   L. H., Klinke, S., Llarrull, L. I., Bonomo, R. A., and Vila, A. J.: The reaction mechanism of
762   metallo-β-lactamases is tuned by the conformation of an active-site mobile loop,
763   Antimicrob. Agents Chemother, 63, e01754-18, https://doi.org/10.1128/AAC.01754-18,
764   2019.

765   Payne, D. J., Hueso-Rodriguez, J. A., Boyd, H., Concha, N. O., Janson, C. A., Gilpin, M.,
766   Bateson, J. H., Cheever, C., Niconovich, N. L., Pearson, S., Rittenhouse, S., Tew, D., Díez,
767   E., Pérez, P., de la Fuente, J., Rees, M., and Rivera-Sagredo, A.: Identification of a series of
768   tricyclic natural products as potent broad-spectrum inhibitors of metallo-β-lactamases,
769   Antimicrob. Agents Chemother., 46, 1880–1886, https://doi.org/10.1128/AAC.46.6.1880-
770   1886.2002, 2002.

771   Pearce, B. J. G., Jabar, S., Loh, C. T., Szabo, M., Graham, B., and Otting, G.: Structure
772   restraints from heteronuclear pseudocontact shifts generated by lanthanide tags at two
773   different sites, J. Biomol. NMR, 68, 19–32, https://doi.org/10.1007/s10858-017-0111-z,
774   2017.

775   Pilla, K. B., Otting, G., and Huber, T.: Protein structure determination by assembling super-
776   secondary structure motifs using pseudocontact shifts, Structure, 25, 559–568,
777   https://doi.org/10.1016/j.str.2017.01.011, 2017.

778 Pintacuda, G., Park, A. Y., Keniry, M. A., Dixon, N. E., and Otting, G.: Lanthanide labeling
779   offers fast NMR approach to 3D structure determinations of protein-protein complexes, J.
780   Am. Chem. Soc., 128, 3696–3702, https://doi.org/10.1021/ja057008z, 2006.

781 Rossi, M.-A., Martinez, V., Hinchliffe, P., Mojica, M. F., Castillo, V., Moreno, D. M., Smith,
782   R., Spellberg, B., Drusano, G. L., Banchio, C., Bonomo, R. A., Spencer, J., Vila, A. J., and
783   Mahler, G.: 2-Mercaptomethyl-thiazolidines use conserved aromatic–S interactions to
784   achieve broad-range inhibition of metallo-β-lactamases, Chem. Sci., 12, 2898–2908,
785   https://doi.org/10.1039/d0sc05172a, 2021.

786 Salimraj, R., Hinchliffe, P., Kosmopoulou, M., Tyrrell, J. M., Brem, J., van Berkel, S. S.,
787   Verma, A., Owens, R. J., McDonough, M. A., Walsh, T. R., Schofield, C. J., and Spencer,
788   J.: Crystal structures of VIM-1 complexes explain active site heterogeneity in VIM-class
789   metallo-β-lactamases, FEBS J., 286, 169–183, https://doi.org/10.1111/febs.14695, 2018.

790 Shishmarev, D. and Otting, G.: How reliable are pseudocontact shifts induced in proteins and
791   ligands by mobile paramagnetic metal tags? A modelling study, J. Biomol. NMR, 56, 203–
792   216, https://doi.org/10.1007/s10858-013-9738-6, 2013.

793 Softley, C. A., Zak, K. M., Bostock, M. J., Fino, R., Zhou, R. X., Kolonko, M., Mejdi-Nitiu,
794   R., Meyer, H., Sattler, M., and Popowicz, G. M.: Structure and molecular recognition
795   mechanism of IMP-13 metallo-β-lactamase, Antimicrob. Agents Chemother., 64, e00123-
796   20, https://doi.org/10.1128/AAC.00123-20, 2020.

797 Su, X.-C., McAndrew, K., Huber, T., and Otting, G.: Lanthanide-binding peptides for NMR
798   measurements of residual dipolar couplings and paramagnetic effects from multiple angles,
799   J. Am. Chem. Soc., 130, 1681–1687, https://doi.org/10.1021/ja076564l, 2008.

800 Toney, J. H., Hammond, G. G., Fitzgerald, P. M., Sharma, N., Balkovec, J. M., Rouen, G. P.,
801   Olson, S. H., Hammond, M. L., Greenlee, M. L., and Gao, Y. D.: Succinic acids as potent
802   inhibitors of plasmid-borne IMP-1 metallo-β-lactamase, J. Biol. Chem., 276, 31913–31918,
803   https://doi.org/10.1074/jbc.M104742200, 2001.

804 van Duin, D., Kaye, K. S., Neuner, E. A., and Bonomo, R. A.: Carbapenem-resistant
805   Enterobacteriaceae: a review of treatment and outcomes, Diagn. Microbiol. Infect. Dis. 75,
806   115−120, https://doi.org/10.1016/j.diagmicrobio.2012.11.009, 2013.

807 Wachino, J., Kanechi, R., Nishino, E., Mochizuki, M., Jin, W., Kimura, K., Kurosaki, H., and
808   Arakawa, Y.: 4-Amino-2-sulfanylbenzoic acid as a potent subclass B3 metallo-β-lactamase-
809   specific inhibitor applicable for distinguishing metallo-β-lactamase subclasses, Antimicrob.
810   Agents Chemother. 63, e01197-19, https://doi.org/10.1128/AAC.01197-19, 2019.

Watanabe, M., S. Iyobe, M. Inoue, and S. Mitsuhashi: Transferable imipenem resistance in *Pseudomonas aeruginosa*, Antimicrob. Agents Chemother. 35, 147–151, https://doi.org/10.1128/AAC.35.1.147, https://doi.org/10.1128/AAC.35.1.147, 1991.

Yagi, H., Pilla, K. B., Maleckis, A., Graham, B., Huber, T., and Otting, G.: Three-dimensional protein fold determination from backbone amide pseudocontact shifts generated by lanthanide tags at multiple sites, Structure, 21, 883–890, https://doi.org/10.1016/j.str.2013.04.001, 2013.

Yamaguchi, Y., Matsueda, S., Matsunaga, K., Takashio, N., Toma-Fukai, S., Yamagata, Y., Shibata, N., Wachino, J., Shibayama, K., Arakawa, Y., and Kurosaki, H.: Crystal structure of IMP-2 metallo-β-lactamase from *Acinetobacter* spp.: comparison of active-site loop structures between IMP-1 and IMP-2, Biol. Pharm. Bull. 38, 96–101, https://doi.org/10.1248/bpb.b14-00594, 2015.

Yamaguchi, Y., Kato, K., Ichimaru, Y., Jin, W., Sakai, M., Abe, M., Wachino, J., Arakawa, Y., Miyagi, Y., Imai, M., Fukuishi, N., Yamagata, Y., Otsuka, M., Fujita, M., and Kurosaki, H.: Crystal structures of metallo-β-lactamase (IMP-1) and its D120E mutant in complexes with citrate and the inhibitory effect of the benzyl group in citrate monobenzyl ester, J. Med. Chem., 64, 10019–10026, https://doi.org/10.1021/acs.jmedchem.1c00308, 2021.

Yamaguchi, H., M. Nukaya, and T. Sawai, T: Sequence of *Klebsiella pneumoniae* RDK4 metallo-β-lactamase, EMBO database accession no. D29636, EMBO, Heidelberg, Germany, 1994.

Zimmermann, K., Joss, D., Müntener, T., Nogueira, E. S., Schäfer, M., Knörr, L., Monnard, F. W., and Häussinger, D.: Localization of ligands within human carbonic anhydrase II using ^{19}F pseudocontact shift analysis, Chem. Sci., 10, 5064–5072, https://doi.org/10.1039/c8sc05683h, 2019.